MDPI

Article

Microvasculature Features Derived from Hybrid EPI MRI in Non-Enhancing Adult-Type Diffuse Glioma Subtypes

Fatemeh Arzanforoosh [1,2], **Sebastian R. van der Voort** [1,2], **Fatih Incekara** [1,3], **Arnaud Vincent** [2,3], **Martin Van den Bent** [2,4], **Johan M. Kros** [2,5], **Marion Smits** [1,2,6] and **Esther A. H. Warnert** [1,2,*]

[1] Department of Radiology and Nuclear Medicine, Erasmus MC, 3015 GD Rotterdam, The Netherlands
[2] Brain Tumor Center, Erasmus MC Cancer Institute, 3015 GD Rotterdam, The Netherlands
[3] Department of Neurosurgery, Erasmus MC, 3015 GD Rotterdam, The Netherlands
[4] Department of Neurology, Erasmus MC, 3015 GD Rotterdam, The Netherlands
[5] Department of Pathology, Erasmus MC, 3000 CB Rotterdam, The Netherlands
[6] Medical Delta, 2629 JH Delft, The Netherlands
[*] Correspondence: e.warnert@erasmusmc.nl

Simple Summary: Reliable insight into tumor microvasculature is important for monitoring disease progression and treatment response. Vessel size imaging (VSI), an emerging MRI technique, has shown great potential in revealing accurate information about microvasculature in gliomas. However, the technique has rarely been used in the clinical setting, as investigated here. Of note, our work was only aimed at non-enhancing tumors. This sets our work apart from other studies investigating tumor microvasculature, typically including enhancing tumors, i.e., tumors in which angiogenesis is already evident macroscopically. Additionally, our findings are of potential clinical relevance for differentiating the most aggressive tumor subtype, glioblastoma, from two other glioma subtypes: oligodendroglioma and astrocytoma. This is particularly challenging when there is no contrast enhancement.

Abstract: In this study, we used the vessel size imaging (VSI) MRI technique to characterize the microvasculature features of three subtypes of adult-type diffuse glioma lacking enhancement. Thirty-eight patients with confirmed non-enhancing glioma were categorized into three subtypes: Oligo (IDH-mut&1p/19q-codeleted), Astro (IDH-mut), and GBM (IDH-wt). The VSI technique provided quantitative maps of cerebral blood volume (CBV), microvasculature (μCBV), and vessel size for each patient. Additionally, tissue samples of 21 patients were histopathologically analyzed, and microvasculature features were quantified. Both MRI- and histology-derived features were compared across the three glioma subtypes with ANOVA or Kruskal–Wallis tests. Group averages of CBV, μCBV, and vessel size were significantly different between the three glioma subtypes ($p < 0.01$). Astro (IDH-mut) had a significantly lower CBV and μCBV compared to Oligo (IDH-mut&1p/19q-codeleted) ($p = 0.004$ and $p = 0.001$, respectively), and a higher average vessel size compared to GBM (IDH-wt) ($p = 0.01$). The histopathological analysis showed that GBM (IDH-wt) possessed vessels with more irregular shapes than the two other subtypes ($p < 0.05$). VSI provides a good insight into the microvasculature characteristics of the three adult-type glioma subtypes even when lacking enhancement. Further investigations into the specificity of VSI to differentiate glioma subtypes are thus warranted.

Keywords: vessel size imaging; microvessel; perfusion imaging; cerebral blood volume; glioma; molecular typing

1. Introduction

Angiogenesis is an essential process for glioma development and growth [1]. In addition to increased vessel density, it also leads to morphologically abnormal vessels

compared to healthy tissue [2]. As the tumor becomes more aggressive, it develops a highly defective vasculature with tortuous vessels of variable diameter and abnormal capillary bed topology, arteriovenous shunting, and microthromboses [3,4]. At this stage, angiogenesis becomes visible with MRI in the form of contrast enhancement. The histopathological features of glioma vasculature, i.e., piling up of endothelial cells, pericytes, and smooth muscle positive mural cells, are traditionally used for predicting tumor malignancy [5].

Three main subtypes of adult-type diffuse glioma are recognized in the 2021 WHO classification of tumors of the central nervous system [6]. These subtypes are: Oligodendroglioma with IDH mutation and 1p/19q-codeletion, Oligo (IDH-mut&1p/19q-codeleted); Astrocytoma with IDH mutation but without 1p/19q-codeletion, Astro (IDH-mut); and Glioblastoma without IDH mutation, i.e., IDH wildtype, GBM (IDH-wt). Among these subtypes, patients with Oligo (IDH-mut&1p/19q-codeleted) have the longest, and patients with GBM (IDH-wt) the shortest, median overall survival (OS) [7].

There are data suggestive of glioma subtype-specific vasculature patterns [3,8]. Glioblastoma is an end-stage tumor in which the overexpression of hypoxia- and angiogenesis-related genes have resulted in sarcomatous vascular structures as well as thrombosis and recanalization [9]. Cha et al. reported differences in the vasculature patterns of blood vessels between oligodendroglioma and astrocytoma [10]. Oligodendroglioma is known to have a unique "chicken-wire" vasculature pattern, while astrocytoma microvasculature more often displays similar features to the normal brain parenchyma.

In recent years, imaging markers derived from clinical or advanced magnetic resonance imaging (MRI) have increasingly been researched to provide insight into tumor vascularization of the whole tumor in a non-invasive manner. This is of particular interest diagnostically in tumors not displaying contrast enhancement because conventional features of angiogenesis are lacking. Vessel size imaging (VSI) is an emerging MRI technique that creates a quantitative map of vessel size, which estimates the mean diameter of vessels in each voxel of the brain MRI scan, in addition to a cerebral blood volume (CBV) map [11,12]. The VSI technique utilizes the dynamic acquisition of both T2-weighted and T2*-weighted images, to follow a bolus of gadolinium-based contrast agent (GBCA) as it passes through the vasculature. Studies have shown that T2-weighted sensitivity peaks for capillary-sized vessels and is used for measuring the microvascular cerebral blood volume (μCBV), while T2*-weighted sensitivity plateaus over a broad range of vessel sizes and has been widely used for measuring the well-known perfusion parameter of CBV [13]. Chakhoyan et al. showed that vessel size and CBV measured with the VSI technique had a good agreement with histopathological measurements of vessel caliber and vessel density in high-grade glioma [14].

While many studies have investigated the value of CBV in predicting tumor angiogenesis, tumor grade, molecular profiles, and overall survival in glioma [15–18], very few studies have explored the potential of vessel size quantification in revealing the vascular characteristics of different glioma subtypes [8,19]. Further, so far and to the best of our knowledge, no study has explored the VSI technique in differentiating microvasculature features in the three most common adult-type diffuse glioma subtypes classified based on the 2021 WHO classification of tumors of the central nervous system: Astro (IDH-mut), Oligo (IDH-mut&1p/19q-codeleted), and GBM (IDH-wt) [6]. This study aimed to explore the glioma lineage-specificity of the blood vessels by VSI, with a particular focus on non-enhancing tumors when angiogenesis is not yet visible on conventional imaging. Additionally, we performed a histopathology analysis of tumor vasculature with the endothelial cell marker CD31 to compare the MRI-based microvascular features in the three glioma subtypes with their histopathological counterparts.

2. Materials and Methods

2.1. Patients

A prospectively collected dataset from the iGENE study, consisting of 44 patients aged 18 years or older, was used for the current analysis. The iGENE study aimed to assess the

value of advanced MRI for diagnosing non-enhancing molecular subtypes of adult-type diffuse glioma. This study was approved by the Institutional Review Board of Erasmus MC, with all patients providing informed written consent to have their information stored and used for research prospectively and retrospectively (MEC-2016-717). All MRI scans were acquired preoperatively, typically one or two days before the surgery. Only patients diagnosed with glioma, confirmed by histopathology after tumor resection or biopsy, were included in the current work. Visual inspection of pre- and postcontrast T1-weighted imaging was performed by an experienced neuroradiologist to ensure that the tumor was indeed non-enhancing. Histopathological examination and molecular subclassification of 1p/19q codeletion status and IDH mutation status were performed as part of the diagnostic routine. The study was initiated prior to the publication of the WHO 2021 classification, but all molecular data were available to classify each tumor based on the WHO 2021 criteria. We excluded 6 patients due to incomplete data or insufficient image quality; therefore, the MRI analysis was performed in 38 patients. Additionally, 21 patients were included for histopathological analysis by an expert neuropathologist who determined that the hematoxylin and eosin (H&E)-stained slides of prepared tissue samples contained sufficient tumor cells.

2.2. MRI Acquisition

All patients underwent 3T MRI scanning (GE, Milwaukee, WI, USA) prior to surgery with a 32-channel head coil. To obtain the microvessel parameters, Hybrid Echo Planar Imaging (HEPI) was used to simultaneously collect both T2-weighted images with spin echo (HEPI-SE) and T2*-weighted images with gradient echo (HEPI-GRE). The acquisition parameters of the HEPI scan were: TR of 1500 ms; TE(GRE)/TE(SE) of 18.6/69 ms; voxel size of $1.9 \times 1.9 \times 4.0$ mm^3; slice thickness of 3.0 mm (with 1.0 mm gap between slices); 120 time points; partial brain coverage with 15 slices placed over the tumor [20]. HEPI was performed with the administration of 7.5 mmol of GBCA (Gadovist, Bayer, Leverkusen, Germany), 20 TRs after the start of the HEPI acquisition. A pre-load bolus of equal size was given 5 min prior to the HEPI scan. The MRI protocol also included high-resolution structural images as part of routine clinical imaging. These were T1-weighted (TE/TR: 2.1/6.1 ms; TI: 450 ms; voxel size: $1.0 \times 1.0 \times 0.5$ mm^3), T2-weighted (TE/TR: 107/10,000 ms; voxel size: $0.5 \times 0.5 \times 3.2$ mm^3), and T2-weighted FLAIR (TE/TR: 106/6000 ms; TI: 1890 ms; voxel size: $0.6 \times 0.5 \times 0.5$ mm^3), all with the field of view covering the entire brain. T1-weighted scans were collected both before GBCA injection (precontrast T1-weighted) and after injection of the pre-load bolus but prior to the HEPI scan (postcontrast T1-weighted). A diffusion-weighted scan, used for estimation of the apparent diffusion coefficient (ADC) required for vessel size measurements, was also included in the protocol with acquisition parameters of TE/TR of 63/5000 ms; voxel size of $1.0 \times 1.0 \times 3.0$ mm^3; 3 b-values of 0, 10, 1000 s/mm^2; and with the field of view covering the entire brain.

2.3. MR Image Pre-Processing

The first four brain volumes of both HEPI-GRE and HEPI-SE were removed to ensure that the signal had reached a steady state. If visually detected, motion artifacts were corrected for both HEPI-GRE and HEPI-SE data, using MC FLIRT (FMRIB's Linear Image Registration Tool, University of Oxford, Oxford, UK), rigidly registering all brain volumes to the fifth brain volume of HEPI-SE [21,22].

In-house code developed in Python 3.6 (http://www.python.org) (accessed on 4 April 2022) was used for acquiring vessel size and CBV maps. Signal–time curves were plotted for each voxel for both HEPI-GRE and HEPI-SE data separately. We excluded voxels exhibiting a drop of fewer than 2 standard deviations of the baseline signal due to the contrast agent passing through, in both HEPI-GRE and HEPI-SE data, to minimize voxels with erroneous

results [23]. Then, HEPI-GRE and HEPI-SE signal–time curves were converted to transverse relaxation rates of $\Delta R_2^*(t)$ and $\Delta R_2(t)$, respectively, using the following equations [13]:

$$\Delta R_2^*(t) = -(1/TE_{GRE}) \times (\ln(S_{GRE}(t)/S_{GRE}(0))), \tag{1}$$

$$\Delta R_2(t) = -(1/TE_{SE}) \times (\ln(S_{SE}(t)/S_{SE}(0))), \tag{2}$$

where TE is the echo time; $S_{GRE}(t)$ and $S_{SE}(t)$ are the signal–time curves of HEPI-GRE and HEPI-SE. Similarly, $S_{GRE}(0)$ and $S_{SE}(0)$ are the baseline signal of the $S_{GRE}(t)$ and $S_{SE}(t)$ for the time prior to the GBCA bolus arrival.

The CBV and µCBV maps were estimated voxelwise from $\Delta R_2^*(t)$ and $\Delta R_2(t)$, respectively, by measuring the trapezoidal integration in the time interval of entrance time (t0) to exit time (t1) of the GBCA bolus:

$$CBV = \int_{t_0}^{t_1} \Delta R_2^*(t)dt \,, \tag{3}$$

$$\mu CBV = \int_{t_0}^{t_1} \Delta R_2(t)dt \,, \tag{4}$$

Normalization of CBV and µCBV maps was performed by dividing all voxels by the mean CBV and µCBV values of normal-appearing white matter voxels in the hemisphere contralateral to the tumor (NAWM-contra) [12]. We will refer to the normalized CBV and µCBV as the CBV and µCBV throughout the rest of the paper.

The estimation of mean vessel size for each voxel was based on the Kiselev model and was obtained by the following equation [12]:

$$\text{Vessel Size} = 0.867(CBV \times ADC)^{1/2}\left[\frac{\Delta R_2^*}{(\Delta R_2)^{3/2}}\right], \tag{5}$$

CBV used in Equation (5) was scaled to the median value of CBV in NAWM-contra of 3.2% [24]. ADC is the apparent diffusion coefficient generated from the diffusion-weighted scan and obtained directly from GE scanner (software version of DV25.0_R01_1451.a). Both ΔR_2^* and ΔR_2 represent the maximum change in the transverse relaxation rates of $\Delta R_2^*(t)$ and $\Delta R_2(t)$, respectively.

It is worth mentioning that no leakage correction algorithms were used in calculating the CBV, µCBV, or vessel size in this study. This is because no or very little contrast agent leakage was observed in the postcontrast T1-weighted image in the tumor area, as per the inclusion criteria; thus, GBCA leakage is not a cause of concern in the current analysis [17]. The in-house developed algorithm of Glioseg was applied on the pre postcontrast T1-weighted, postcontrast T1-weighted, T2-weighted, and T2-weighted FLAIR images to generate a 3D tumor mask (Figure 1A). This automatic tumor segmentation was performed by five different algorithms [25–28] (details described in Appendix A).

A normal-appearing white matter mask from the hemisphere contralateral to the tumor (NAWM-contra) was extracted for CBV and µCBV normalization, as described above. To obtain the NAWM-contra mask, first, FAST in FSL (FMRIB's Automated Segmentation Tool, Version 6.0.5) was applied on the brain-extracted precontrast T1-weighted image to generate probability maps of white matter, grey matter, and cerebrospinal fluid [29]. The white matter probability map from the hemisphere contralateral to the tumor was then manually selected, and, to minimize partial volume effects, binarized with a probability threshold of 0.9 and eroded with FSLMATHS in FSL using a kernel size of $3 \times 3 \times 3$ mm^3.
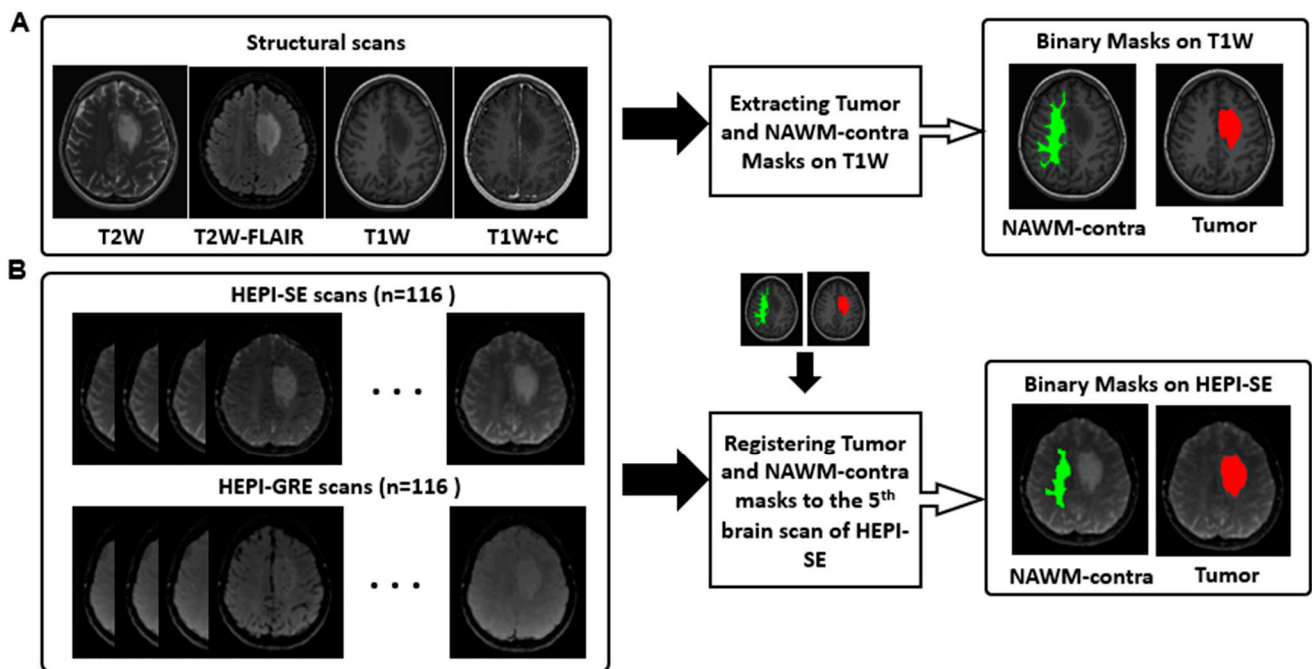
Figure 1. Preprocessing workflow. (**A**) T2-weighted (T2W), T2-weighted FLAIR (T2W-FLAIR), precontrast T1-weighted (T1W) and postcontrast T1-weighted (T1W + C) images are used for extracting binary masks of tumor (highlighted in red) and NAWM-contra (highlighted in green); (**B**) brain scans of HEPI-GRE and HEPI-SE; the generated binary masks of tumor (highlighted in red) and NAWM-contra (highlighted in green) are transferred from structural space to HEPI space. The overlaid NAWM-contra and tumor masks have a numerical value of one, with distinct colors employed solely to enhance visual differentiation.

Tumor and NAWM-contra masks were then registered to the HEPI space. For this, the brain-extracted precontrast T1-weighted image was linearly registered to the fifth brain volume of HEPI-SE (after preprocessing) using Elastix (version 4.8) [30]. Then, the same transformation matrix was used to transfer the NAWM-contra and tumor masks to the HEPI-SE space (Figure 1B).

2.4. Histopathological Analysis

Histology slides produced from paraffin-embedded tumor biopsies were routinely stained for H&E and adjacent cuts were immunohistochemically stained for CD31, a marker for endothelial cells. For the virtual microscopy analysis, the slides were scanned with the Hamamatsu Nanozoomer 2.0-HT C9600-12 (Hamamatsu Photonics, Hamamatsu City, Shizuoka Prefecture, Japan) to obtain whole-slide high-resolution images.

The H&E-stained slides of the prepared tissue samples were examined by an experienced neuropathologist for tumor content. For the histopathological analysis, two regions of interest (ROIs), representative of vasculature features in the whole tissue, were selected by the experienced neuropathologist for each tissue sample. In these ROIs, all positively stained endothelial cells and vessel structures were segmented and quantified based on the CAIMAN algorithm (http://www.caiman.org.uk) (accessed on 2 February 2022) [31]. The quantification included vessel density, average vessel radius, and average vessel roundness for each patient. Vessel density was estimated by measuring the area of the stained vessels in both ROIs divided by the total area of the ROIs. Each vessel radius in the ROIs was measured with the CAIMAN algorithm and averaged across the ROIs. Vessel roundness is a metric describing how elongated the object is together with how smooth or crenated the external boundary of each vessel is. A roundness of 1 reflects a vessel with a completely circular shape, while a higher value of this parameter is associated with a more irregular vessel shape.

2.5. Statistical Analysis

Mean and median values of MRI-derived CBV, μCBV, and vessel size were computed in the tumor area for each patient. A hot spot approach was also used where, initially, clusters of voxels in the 90th percentile within the tumor mask were identified. The values within these clusters were averaged and reported for each parameter. Mean, median, and hot spot values were measured across all clusters together and were then averaged for each of the three glioma subtypes separately. Additionally, the histology-derived parameters of vessel density, vessel radius, and vessel roundness were first measured for each tissue sample in the two predefined regions of interest (ROIs). Then, these parameters were group-averaged for each glioma subtype. It is noteworthy that selected ROIs were quite small and homogenously stained; thus, only the mean of the histology-derived parameters was obtained in each ROI.

All statistical analyses were performed with the statistics package of SciPy (version 1.10.1) in python version 3.6. For group comparison, first, the normality of both the MRI-derived and histology-derived parameters of each subtype was examined with the Shapiro–Wilk test. For normally distributed data, the one-way analysis of variance test (ANOVA) was used. If the group means were significantly different among glioma subtypes, a post hoc Tukey honestly significant difference (HSD) test was performed to identify the groups which are responsible for the significant variation. For non-normally distributed data, the Kruskal–Wallis (KW) test was used and, if it yielded a statistically significant result, it was followed by a post hoc Dunn's test using a Bonferroni correction. A *p*-value of 0.05 or lower was considered significant in all tests.

3. Results

3.1. Patient Characteristics

Thirty-eight patients (median age of 42 years; age range 22–77 years; 25 men) were included, in 21 of whom (median age of 42 years; age range 28–71 years; 17 men) sufficient tissue was available for the histopathological analysis. Eighteen patients were diagnosed with Oligo (IDH-mut&1p/19q-codeleted), 13 with Astro (IDH-mut), and 7 with Glioblastoma (IDH-wt) (Table 1).

Table 1. Patient characteristics and histopathological grade based on the WHO 2021 classification of tumors of the central nervous system [6]. Patient characteristics with additional histopathological tissue analysis in brackets.

| Tumor Subtype	Grade 2	Grade 3	Grade 4	Total	Sex	Age (Years)
Oligo (IDH-mut&1p/19q-codeleted)	15 (6)	3 (2)	- -	18 (8)	13M/5F (7M/1F)	40 ± 12 (43 ± 13)
Astro (IDH-mut)	9 (7)	4 (-)	- (-)	13 (7)	5M/8F (4M/3F)	36 ± 8 (35 ± 6)
GBM (IDH-wt)	- (-)	- (-)	7 (6)	7 (6)	7M/0F (6M/0F)	60 ± 10 (59 ± 8)

3.2. MRI-Based Measurements

The group averages of CBV, μCBV, and vessel size for each of the three glioma subtypes are provided in Table 2. Mean and median measurements of CBV, μCBV, and vessel size were significantly different between the three subtypes ($p < 0.05$). Hot spot measurements showed a significant difference between the three subtypes only for μCBV.

Table 2. Group averages of CBV, μCBV, and vessel size in the three glioma subtypes: Oligo (IDH-mut&1p/19q-codeleted), Astro (IDH-mut), and GBM (IDH-wt). [a]: one-way ANOVA test; [b]: Kruskal–Wallis test. The bold formatting indicates a significant *p*-value.

		Oligo (IDH-mut&1p/19q-codeleted)	Astro (IDH-mut)	GBM (IDH-wt)	*p*-Value
MRI-derived parameters					
CBV (%)	Mean (std)	1.43 (0.44)	0.96 (0.36)	1.20 (0.39)	**0.01 [a]**
	Median (std)	1.17 (0.36)	0.70 (0.18)	0.92 (0.37)	**<0.001 [b]**
	Hot spot (std)	3.31 (1.14)	2.79 (1.71)	3.34 (0.85)	0.13
μCBV (%)	Mean (std)	1.45 (0.29)	0.86 (0.26)	1.36 (0.71)	**<0.001 [b]**
	Median (std)	1.31 (0.25)	0.74 (0.21)	1.29 (0.73)	**<0.001 [b]**
	Hot spot (std)	2.37 (0.60)	1.62 (0.77)	2.22 (0.83)	**0.02 [a]**
Vessel size (μm)	Mean (std)	12.48 (2.61)	15.55 (5.10)	10.33 (3.62)	**0.01 [a]**
	Median (std)	10.18 (2.02)	10.91 (2.47)	7.02 (2.32)	**0.002 [a]**
	Hot spot (std)	44.91 (15.55)	78.85 (46.48)	53.81 (34.96)	0.06 [a]
Histopathology-derived parameters					
Vessel density	Mean (std)	3.69 (1.64)	3.45 (2.09)	6.47 (2.74)	**0.03 [a]**
Vessel radius (μm)	Mean (std)	8.61 (1.92)	8.72 (1.82)	7.68 (1.70)	0.55 [b]
Vessel roundness	Mean (std)	1.23 (0.03)	1.20 (0.06)	1.34 (0.03)	**<0.001 [a]**

Pairwise comparison of mean CBV and mean μCBV showed a significant difference between Oligo (IDH-mut&1p/19q-codeleted) and Astro (IDH-mut) (p = 0.004 and $p < 0.001$, respectively), with Oligo (IDH-mut&1p/19q-codeleted) having significantly higher values for both these parameters.

In addition, μCBV showed a trend of being higher in GBM (IDH-wt) compared to Astro (IDH-mut); however, this did not reach the statistically significant level (p = 0.12) (Figure 2).
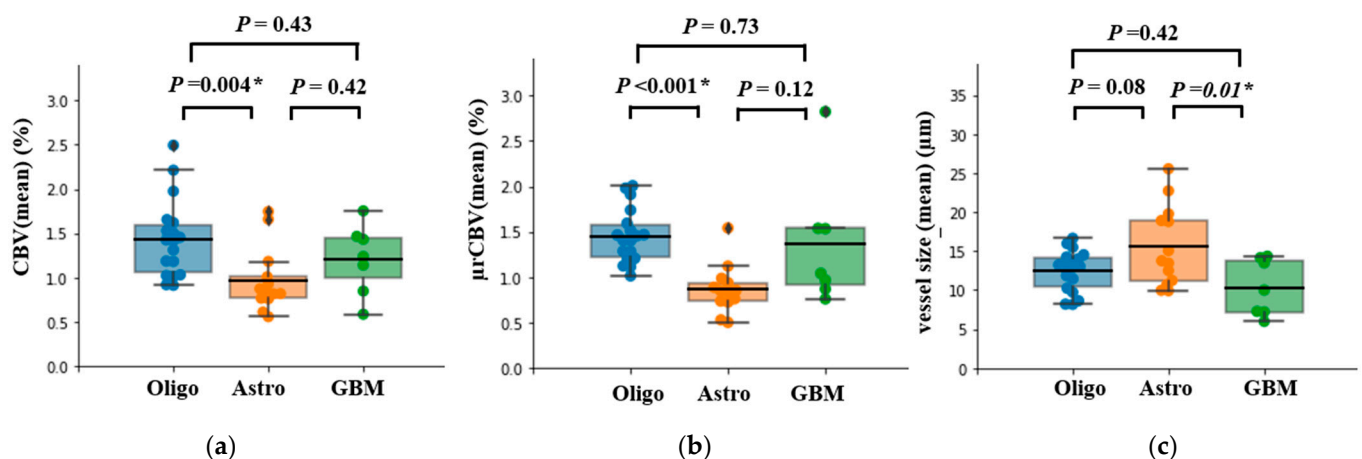

Figure 2. Box plot of MRI-derived measurements of (**a**) CBV, (**b**) μCBV, and (**c**) vessel size, with mean bar for the three glioma subtypes Oligo (IDH-mut &1p/19q codeleted), Astro (IDH-mut), and GBM (IDH-wt). Tukey HSD test or Dunn's test using a Bonferroni correction was used for pairwise statistical analysis. '*' indicates significant difference between two subtypes accompanied by the exact *p*-value.

A pairwise comparison of mean vessel size revealed a significantly lower value for GBM (IDH-wt) in comparison to Astro (IDH-mut) (p = 0.01). Although there was a trend for Oligo (IDH-mut&1p/19q-codeleted) to have a smaller mean vessel size compared

to Astro (IDH-mut) ($p = 0.08$), this difference did not reach the statistical significance level (Figure 2c). No difference was observed in CBV, μCBV, and vessel size between Oligo (IDH-mut&1p/19q-codeleted) and GBM (IDH-wt) ($p = 0.43$, $p = 0.73$, and $p = 0.42$, respectively).

Figure 3 illustrates exemplary slices of CBV, μCBV, and vessel size maps for a representative patient of each subtype. In Oligo (IDH-mut&1p/19q-codeleted) and GBM (IDH-wt), both CBV and μCBV are distinctly high in the tumor area, while vessel size maps show low-to-intermediate intensity in the tumor area. In Astro (IDH-mut), the reverse is seen: CBV and μCBV are evidently low in the tumor area, while the vessel size map displays several hot spots in the tumor area.
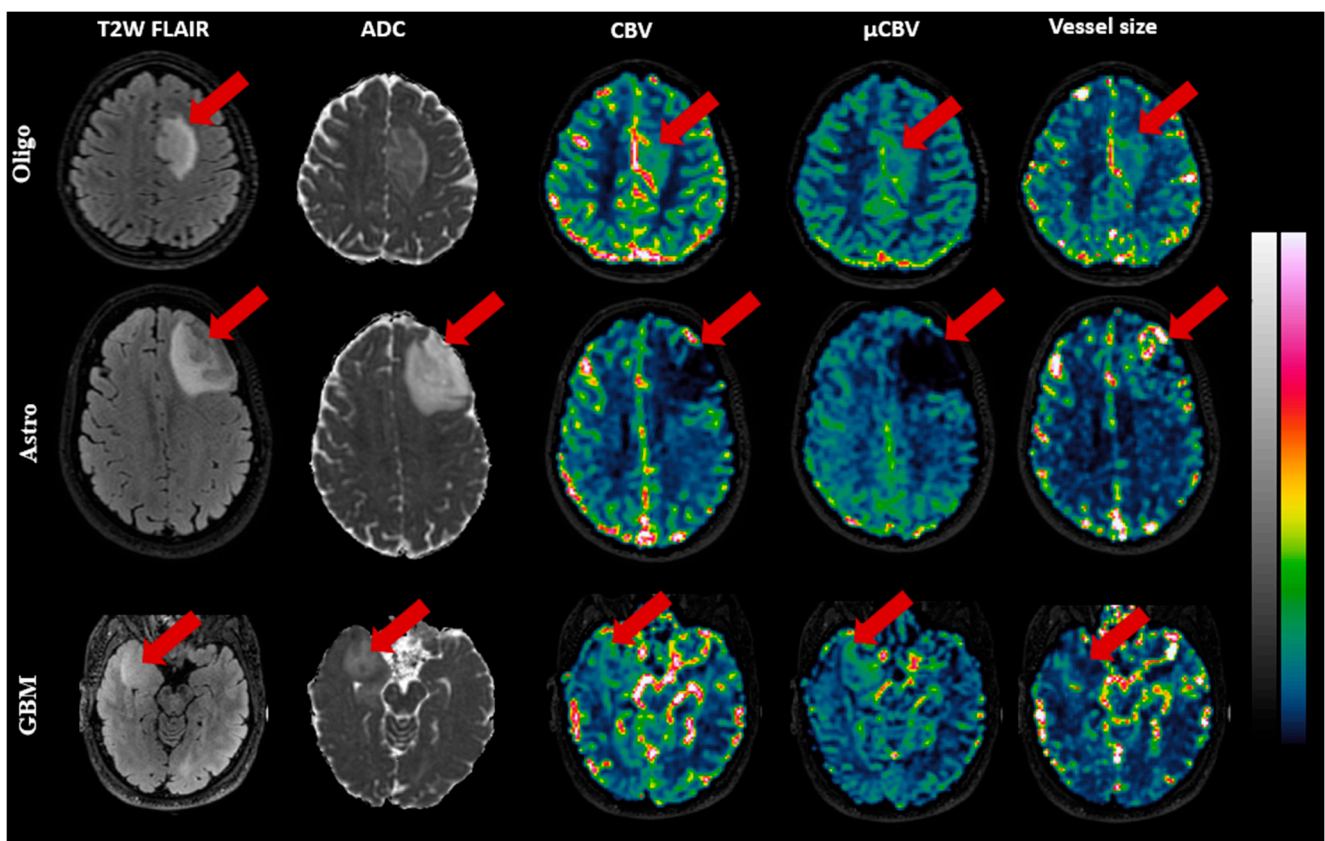
Figure 3. Exemplary MR images of three patients, Oligo (IDH-mut &1p/19q co-deleted), Astro (IDH-mut), and GBM (IDH-wt), respectively, from top to bottom. The images (with color bars on the right) from left to right, respectively, are: T2W-FLAIR, ADC (0–1 μm^2/s), CBV(0–10%), μCBV(0–10%), and vessel size (0–100 μm), with the red arrow pointing to the tumor.

### 3.3. Histology-Derived Measurements

The results of the histopathological analyses are shown in Figure 4. There was a significant difference in vessel density between the three subtypes ($p = 0.03$); however, the pairwise comparison only showed a trend of higher vessel density in GBM (IDH-wt) compared to Oligo (IDH-mut&1p/19q-codeleted) ($p = 0.06$). No statistically significant difference was found in vessel radius between each of the three glioma subtypes. Vessel morphology, however, was significantly different in GBM (IDH-wt) compared to both Oligo (IDH-mut&1p/19q-codeleted) ($p = 0.02$) and Astro (IDH-mut) ($p = 0.03$), with GBM (IDH-wt) having the least round-shaped microvasculature.
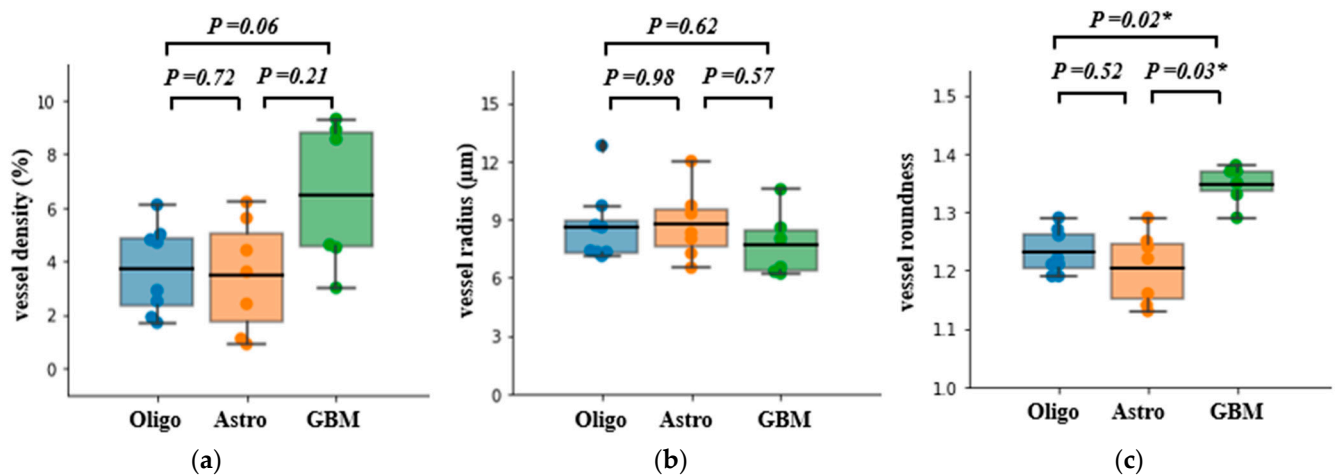
Figure 4. Box plot of histology-derived measurements: (**a**) vessel density, (**b**) vessel radius, and (**c**) vessel roundness, with mean bar for the three glioma subtypes Oligo (IDH-mut &1p/19q codeleted), Astro (IDH-mut), and GBM (IDH-wt). Tukey honestly significant difference (HSD) test or Dunn's test using a Bonferroni correction was used for pairwise statistical analysis. '*' indicates a significant difference between two subtypes accompanied by the exact *p*-value.

4. Discussion

In this study, we determined the microvascular characteristics of the three adult-type diffuse glioma subtypes Astro (IDH-mut), Oligo (IDH-mut&1p/19q-codeleted), and GBM (IDH-wt) showing no contrast-enhancement on MRI. Even in the absence of contrast-enhancement—a characteristic macroscopic feature of angiogenesis—there was a significant difference between the three glioma subtypes in MRI-based CBV, μCBV, and vessel size measurements. Moreover, histopathological analysis of the tumor vasculature with the endothelial cell marker CD31 suggested that the morphology of microvasculature in the GBM (IDH-wt) subtype was different from the other two subtypes, having more elongated and crenated morphology. Oligo (IDH-mut&1p/19q-codeleted) showed significantly higher CBV and μCBV compared to Astro (IDH-mut). This finding is in accordance with previous studies [15,16]. Both subtypes are IDH-mutant glioma, but the microvascular proliferation in 1p/19q-codeleted tumors is more common than in 1p/19q intact tumors [32]. Moreover, the Oligo (IDH-mut&1p/19q-codeleted) subtype is typically characterized by small, branching, chicken wire-like blood vessels in histology [10]. This pattern was also observed in most of the stained tissue slides of Oligo (IDH-mut&1p/19q-codeleted) (Figure 5) and may therefore underlie the MRI findings, as the susceptibility contrast measured with CBV is not only sensitive to vessel density, but also to the size, shape, and orientation of the blood vessels [8,10,11].
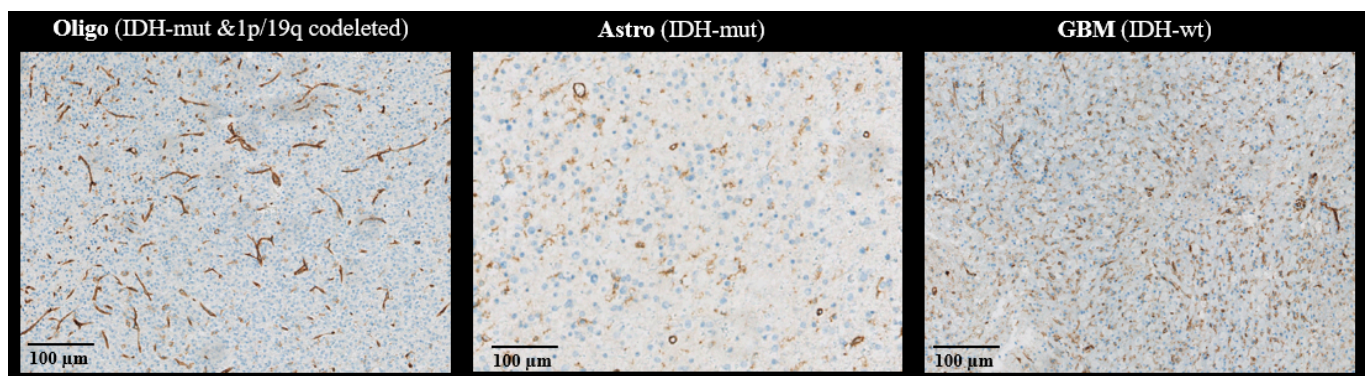
Figure 5. Exemplary CD31-stained tissue of three patients with Oligo (IDH-mut &1p/19q co-deleted), Astro (IDH-mut), and GBM (IDH-wt), from left to right.

The quantitative tissue analysis performed with the CAIMAN algorithm, however, showed hardly any difference in microvascularization between the Oligo (IDH-mut&1p/19q-codeleted) and Astro (IDH-mut) glioma subtypes. A possible explanation for this seemingly contradictory finding is that the CAIMAN algorithm segments and counts stained objects in the slices that are not necessarily blood vessels. Previous studies have reported that while the CD31 antibody is useful for marking tumor angiogenesis, it can also stain non-vascular cells within soft tissue tumors and lead to errors in the analysis [33]. The GBM (IDH-wt) subtype showed a significantly smaller vessel size, as measured with MRI compared to Astro (IDH-mut), a finding that may be of use in clinical practice to non-invasively identify this most aggressive glioma subtype before surgery. In the literature, the reported microvasculature features in GBMs have been conflicting so far. While in many studies dilated glomeruloid-type vessels and microvascular proliferation are linked with GBM [34], it has been shown that vessels in these tumors may be similar to those in the normal brain parenchyma [35]. However, the vessel lumina of high-grade glioma may also narrow because of increasing numbers of their cellular constituents, due to microvascular proliferation [36]. Our histopathological findings support the latter in demonstrating that in GBM (IDH-wt) was the greatest loss of circular shapes of the vessels compared to Astro (IDH-mut) and Oligo (IDH-mut&1p/19q-codeleted), which is characteristic of GBM and potentially the cause of finding a decreased vessel size on MRI. It is worth noting that here, we focused on non-enhancing GBM (IDH-wt), which is clinically highly relevant as only a small proportion of GBMs (IDH-wt) do not enhance and may mimic lower grade tumors. Our findings, which may seem contradictory to some of the previous literature, may be thus related to the selection of these tumors. Additionally, we used the molecular classification for diagnosing GBM (IDH-wt) rather than histopathology, which removes the circularity between the empirical (tissue) measurements and the ground truth, which for histopathological diagnosis includes vessel characteristics. Again, this could also underline differences between our findings and those reported in the (older) literature.

We do know from the literature that IDH wild-type glioma correlates with an overexpression of angiogenesis-related genes, eventually resulting in increased perfusion [9]. Our study showing a trend for both CBV and μCBV, as measured with MRI, as well as vessel density measured in tissue to be higher in GBM (IDH-wt) compared to Astro (IDH-mut), is in line with this finding of overexpressed angiogenesis-related genes. That these differences did not reach the statistically significant level might be explained by the small sample size ($n = 7$) in combination with the large observed heterogeneity of these parameters in GBM (IDH-wt) [15]. Again, it should be noted here that the GBM (IDH-wt) subtype included in the present study was non-enhancing lesions and therefore less typical for the GBMs that come with extensive microvascular proliferation.

Our study had some limitations. The iGENE study was designed to investigate non-enhancing gliomas, which are typically lower grade gliomas; therefore, a smaller number of patients were diagnosed with GBM (IDH-wt). The current work is therefore of an exploratory nature because of the relatively small, unequally distributed sample size. However, our findings can serve as a good starting point for the validation of VSI in a larger cohort to investigate whether VSI could provide an effective tool for the diagnosis of non-enhancing adult-type diffuse glioma subtypes. Another limitation of this study is that not all patients' tissue samples were available for histopathological analysis. Finally, the biopsy location was unknown for the included samples; thus, regional heterogeneity within the tumors could not be accounted for in the histopathological analysis. However, the tissue findings were broadly in line with the MRI-based measurements.

5. Conclusions

In summary, this exploratory work evaluated how VSI can provide information about the microvasculature features of the three subtypes of non-enhancing adult-type diffuse glioma. From a clinical perspective, our findings are of potential interest for differentiating the most aggressive tumor subtype, GBM (IDH-wt), from the Astro (IDH-mut) subtype,

requiring prompt treatment amongst this subset of non-enhancing tumors with otherwise low-grade appearance. Our findings offer direction for future work aimed at confirming these findings in a larger validation cohort, preferably with targeted biopsies, to more precisely correlate MRI findings with tissue characteristics.

Appendix A

Glioseg: a pipeline for automated registration and tumor segmentation.

As a first step, all scans of pre- and postcontrast T1-weighted, T2-weighted, and T2-weighted FLAIR are converted from DICOM files to NifTI files using dcm2niix version v1.0.20211006 [37]. Bias fields are estimated based on the precontrast T1-weighted (T1w) scan using N4 bias-field correction [38], and the estimated bias field from the T1w scan is used to correct the bias in all other scans. All scans are subsequently resampled to ensure they are the same size, fit within the same field of view, and have the same approximate center.

To perform the resampling of all scans, first, all scans are reoriented to the MNI orientation. Brain masks are created for all scans using HD-BET [39] or FSL BET [40]. HD-BET is preferred, but for scans with a limited field of view (FOV) or large voxel size (low resolution), HD-BET tends to fail. Therefore, for scans with less than 256 slices in either the orthogonal or coronal direction or 20 slices in the axial direction, FSL-BET is used to generate the brain masks. In these cases, FSL-BET is used with a fractional intensity threshold of 0.4, and the padding option ("−Z") in the z-direction is used to account for the limited FOV. Then, the best resolution (i.e., the smallest voxel size) and the largest field of view over all scans are determined in each direction. This is carried out for each direction individually to ensure that there is no information loss during the resampling. Then, all scans are resampled to the determined voxel size and FOV. The origins of all scans are also shifted during the resampling such that the center of mass of the brain mask of each scan aligns with the center of mass of the brain mask of the MNI152 atlas. After resampling, brain masks are produced again based on the resampled scans, since the scans are now available in a higher (resampled) resolution.

The next step is to register all scans to the MNI ICBM 152 non-linear symmetric atlas version 2009a [41]. Registration is performed using itk-elastix (Version 0.15.0), based on the Elastix toolbox [30,42]. First, all images are groupwise registered to each other to ensure that the images of the patient align. This groupwise registration is carried out in two steps. In the first step, only the brain masks are groupwise registered. We use the

PCAMetric2, with an EulerStack transform in Elastix. For the second step, the images themselves are used in the groupwise registration, with the brain masks acting as a mask for the registration. Once again, a EulerStackTransform with PCAMetric2 is used. In this second step, all images are groupwise registered except for the T2-weighted FLAIR scan (T2w-FLAIR). We found that the T2w-FLAIR tended to misalign during the second step of the groupwise registration. Therefore, after all the scans (except the T2w-FLAIR) were groupwise registered, the T2w-FLAIR is then registered to the other scans (after they are transformed). The T2w-FLAIR is used as the moving image; all other scans are used as the fixed images. A MultiMetricMultiResolutionRegistration is used with an affine transform and the AdvancedMattesMultualInformation as the metric.

Now that all scans are registered to each other, they are then registered to the atlas. In the first step, the brain masks of the scans are used as moving images and the brain mask of the atlas is used as the fixed image. A EulerTransform is used, with the AdvancedMattesMutualInformation metric. In the second step, the scans themselves are used as moving images, and the T1-weighted and T2-weighted versions of the atlas are used as fixed images. All combinations between the scans and two versions of the atlas are used in a MultiMetricMultiResolutionRegistration. All Elastix parameter files are available upon request.

For every registration/transformation, the transformation parameters are saved. The inverse of each transformation is also determined and saved so that the final segmentations can be transformed back to the original space.

The automatic tumor segmentation is performed using five different segmentation networks:

- nnUNet Task 001 [28];
- nnUNet Task 082 [28];
- HD-GLIO [27,28];
- The winning submission of the Brats 2021 challenge [26];
- DeepScan [25].

All of these models are publicly available. The two nnUNet tasks are available at https://github.com/MIC-DKFZ/nnUNet (accessed on 22 February 2023). HD-GLIO is available at https://github.com/NeuroAI-HD/HD-GLIO (accessed on 22 February 2023). The winning submission of the Brats 2021 challenge is available at https://github.com/rixez/Brats21_KAIST_MRI_Lab (accessed on 22 February 2023). DeepScan is available at https://hub.docker.com/r/brats/scan-20 (accessed on 22 February 2023).

Scans are preprocessed to prepare them according to the requirements set by the different methods. First, we select only the precontrast T1-weighted, postcontrast T1-weighted, T2-weighted and T2-weighted FLAIR for the automatic tumor segmentation. A combined brain mask is produced by uniting the brain masks of the scans. This combined brain mask is then used to skull-strip the scans, as this is a requirement for all methods. Additionally, for the DeepScan method, the scans need to be provided and registered to the SRI24 atlas [43]. We previously registered the MNI152 to the SRI24 atlas, and the obtained transformation file is used to transform the scans to the SRI24 atlas. All the different methods are then applied to the pre-processed scans.

Once the methods have finished segmenting the scans, the resulting segmentations are post-processed. First, the result from the DeepScan algorithm is transformed back to MNI152 space. Second, for all methods, the labels are set such that label 1 is T2w-FLAIR hyperintensities/edema, label 2 is necrosis, and label 3 is enhancing tumor. A threshold is set on each segmentation that at least 1000 voxels should be segmented for that segmentation method to be taken into account. If none of the segmentation methods segment at least 1000 voxels, this threshold is reduced to 5000 voxels. This is to prevent under-segmentation in case one or two methods cannot find the tumor, but the other methods can. The individual segmentations (if they pass the threshold) are then combined using the multi-label STAPLE algorithm [44] as well as a simple majority vote. The user can select which ensembled segmentation they prefer.

As a last step, the tumor segmentations are transformed back to the original space using the inversed transform parameters. This allows for the processing of the data in the original space, avoiding artifacts introduced by the resampling/transforming of the scans.

References

1. Lebelt, A.; Dziecioł, J.; Guzińska-Ustymowicz, K.; Lemancewicz, D.; Zimnoch, L.; Czykier, E. Angiogenesis in Gliomas. *Folia Histochem. Cytobiol.* **2008**, *46*, 69–72. [CrossRef]
2. Plate, K.H.; Mennel, H.D. Vascular Morphology and Angiogenesis in Glial Tumors. *Exp. Toxicol. Pathol.* **1995**, *47*, 89–94. [CrossRef]
3. Chen, W.; He, D.; Li, Z.; Zhang, X.; Pan, D.; Chen, G. Overexpression of Vascular Endothelial Growth Factor Indicates Poor Outcomes of Glioma: A Systematic Review and Meta-Analysis. *Int. J. Clin. Exp. Med.* **2015**, *8*, 8709–8719.
4. Emblem, K.E.; Nedregaard, B.; Nome, T.; Due-Tonnessen, P.; Hald, J.K.; Scheie, D.; Borota, O.C.; Cvancarova, M.; Bjornerud, A. Glioma Grading by Using Histogram Analysis of Blood Volume Heterogeneity from MR-Derived Cerebral Blood Volume Maps. *Radiology* **2008**, *247*, 808–817. [CrossRef] [PubMed]
5. Komori, T. AI Neuropathologist: An Innovative Technology Enabling a Faultless Pathological Diagnosis? *Neuro-Oncology* **2021**, *23*, 1–2. [CrossRef] [PubMed]
6. Louis, D.N.; Perry, A.; Wesseling, P.; Brat, D.J.; Cree, I.A.; Figarella-Branger, D.; Hawkins, C.; Ng, H.K.; Pfister, S.M.; Reifenberger, G.; et al. The 2021 WHO Classification of Tumors of the Central Nervous System: A Summary. *Neuro-Oncology* **2021**, *23*, 1231–1251. [CrossRef]
7. Dubbink, H.J.; Atmodimedjo, P.N.; Kros, J.M.; French, P.J.; Sanson, M.; Idbaih, A.; Wesseling, P.; Enting, R.; Spliet, W.; Tijssen, C.; et al. Molecular Classification of Anaplastic Oligodendroglioma Using Next-Generation Sequencing: A Report of the Prospective Randomized EORTC Brain Tumor Group 26951 Phase III Trial. *Neuro-Oncology* **2016**, *18*, 388–400. [CrossRef] [PubMed]
8. Guo, H.; Kang, H.; Tong, H.; Du, X.; Liu, H.; Tan, Y.; Yang, Y.; Wang, S.; Zhang, W. Microvascular Characteristics of Lower-Grade Diffuse Gliomas: Investigating Vessel Size Imaging for Differentiating Grades and Subtypes. *Eur. Radiol.* **2019**, *29*, 1893–1902. [CrossRef] [PubMed]
9. Kickingereder, P.; Sahm, F.; Radbruch, A.; Wick, W.; Heiland, S.; von Deimling, A.; Bendszus, M.; Wiestler, B. IDH Mutation Status Is Associated with a Distinct Hypoxia/Angiogenesis Transcriptome Signature Which Is Non-Invasively Predictable with RCBV Imaging in Human Glioma. *Sci. Rep.* **2015**, *5*, 16238. [CrossRef]
10. Cha, S.; Tihan, T.; Crawford, F.; Fischbein, N.J.; Chang, S.; Bollen, A.; Nelson, S.J.; Prados, M.; Berger, M.S.; Dillon, W.P. Differentiation of Low-Grade Oligodendrogliomas from Low-Grade Astrocytomas by Using Quantitative Blood-Volume Measurements Derived from Dynamic Susceptibility Contrast-Enhanced MR Imaging. *AJNR Am. J. Neuroradiol.* **2005**, *26*, 266–273.
11. Kellner, E.; Breyer, T.; Gall, P.; Müller, K.; Trippel, M.; Staszewski, O.; Stein, F.; Saborowski, O.; Dyakova, O.; Urbach, H.; et al. MR Evaluation of Vessel Size Imaging of Human Gliomas: Validation by Histopathology. *J. Magn. Reson. Imaging* **2015**, *42*, 1117–1125. [CrossRef]
12. Kiselev, V.G.; Strecker, R.; Ziyeh, S.; Speck, O.; Hennig, J. Vessel Size Imaging in Humans. *Magn. Reson. Med.* **2005**, *53*, 553–563. [CrossRef] [PubMed]
13. Shiroishi, M.S.; Castellazzi, G.; Boxerman, J.L.; D'Amore, F.; Essig, M.; Nguyen, T.B.; Provenzale, J.M.; Enterline, D.S.; Anzalone, N.; Dörfler, A.; et al. Principles of T2∗-Weighted Dynamic Susceptibility Contrast MRI Technique in Brain Tumor Imaging. *J. Magn. Reson. Imaging* **2015**, *41*, 296–313. [CrossRef]
14. Chakhoyan, A.; Yao, J.; Leu, K.; Pope, W.B.; Salamon, N.; Yong, W.; Lai, A.; Nghiemphu, P.L.; Everson, R.G.; Prins, R.M.; et al. Validation of Vessel Size Imaging (VSI) in High-Grade Human Gliomas Using Magnetic Resonance Imaging, Image-Guided Biopsies, and Quantitative Immunohistochemistry. *Sci. Rep.* **2019**, *9*, 2846. [CrossRef] [PubMed]
15. Pruis, I.J.; Koene, S.R.; van der Voort, S.R.; Incekara, F.; Vincent, A.J.P.E.; van den Bent, M.J.; Lycklama à Nijeholt, G.J.; Nandoe Tewarie, R.D.S.; Veldhuijzen van Zanten, S.E.M.; Smits, M. Noninvasive Differentiation of Molecular Subtypes of Adult Nonenhancing Glioma Using MRI Perfusion and Diffusion Parameters. *Neuro-Oncol. Adv.* **2022**, *4*, vdac023. [CrossRef] [PubMed]
16. Leu, K.; Ott, G.A.; Lai, A.; Nghiemphu, P.L.; Pope, W.B.; Yong, W.H.; Liau, L.M.; Cloughesy, T.F.; Ellingson, B.M. Perfusion and Diffusion MRI Signatures in Histologic and Genetic Subtypes of WHO Grade II–III Diffuse Gliomas. *J. Neuro-Oncol.* **2017**, *134*, 177–188. [CrossRef]
17. Arzanforoosh, F.; Croal, P.L.; van Garderen, K.A.; Smits, M.; Chappell, M.A.; Warnert, E.A.H. Effect of Applying Leakage Correction on RCBV Measurement Derived From DSC-MRI in Enhancing and Nonenhancing Glioma. *Front. Oncol.* **2021**, *11*, 648528. [CrossRef]
18. Lemasson, B.; Chenevert, T.L.; Lawrence, T.S.; Tsien, C.; Sundgren, P.C.; Meyer, C.R.; Junck, L.; Boes, J.; Galbán, S.; Johnson, T.D.; et al. Impact of Perfusion Map Analysis on Early Survival Prediction Accuracy in Glioma Patients. *Transl. Oncol.* **2013**, *6*, 766–774. [CrossRef]
19. Kang, H.Y.; Xiao, H.L.; Chen, J.H.; Tan, Y.; Chen, X.; Xie, T.; Fang, J.Q.; Wang, S.; Yang, Y.; Zhang, W.G. Comparison of the Effect of Vessel Size Imaging and Cerebral Blood Volume Derived from Perfusion MR Imaging on Glioma Grading. *Am. J. Neuroradiol.* **2016**, *37*, 51–57. [CrossRef]

20. Ferreira, P.F.; Gatehouse, P.D.; Firmin, D.N. Myocardial First-Pass Perfusion Imaging with Hybrid-EPI: Frequency-Offsets and Potential Artefacts. *J. Cardiovasc. Magn. Reson.* **2012**, *14*, 44. [CrossRef]

21. Jenkinson, M. Improved Optimization for the Robust and Accurate Linear Registration and Motion Correction of Brain Images. *Neuroimage* **2002**, *17*, 825–841. [CrossRef] [PubMed]

22. Jenkinson, M.; Smith, S. A Global Optimisation Method for Robust Affine Registration of Brain Images. *Med. Image Anal.* **2001**, *5*, 143–156. [CrossRef] [PubMed]

23. Bell, L.C.; Stokes, A.M.; Quarles, C.C. Analysis of Postprocessing Steps for Residue Function Dependent Dynamic Susceptibility Contrast (DSC)-MRI Biomarkers and Their Clinical Impact on Glioma Grading for Both 1.5 and 3T. *J. Magn. Reson. Imaging* **2020**, *51*, 547–553. [CrossRef]

24. Leenders, K.L.; Perani, D.; Lammertsma, A.A.; Heather, J.D.; Buckingham, P.; Jones, T.; Healy, M.J.R.; Gibbs, J.M.; Wise, R.J.S.; Hatazawa, J.; et al. Cerebral Blood Flow, Blood Volume And Oxygen Utilization. *Brain* **1990**, *113*, 27–47. [CrossRef] [PubMed]

25. McKinley, R.; Rebsamen, M.; Dätwyler, K.; Meier, R.; Radojewski, P.; Wiest, R. Uncertainty-Driven Refinement of Tumor-Core Segmentation Using 3D-to-2D Networks with Label Uncertainty. In *Brainlesion: Glioma, Multiple Sclerosis, Stroke and Traumatic Brain Injuries*; Springer: Cham, Switzerland, 2021; pp. 401–411.

26. Luu, H.M.; Park, S.-H. Extending Nn-UNet for Brain Tumor Segmentation. In *Brainlesion: Glioma, Multiple Sclerosis, Stroke and Traumatic Brain Injuries*; Springer: Cham, Switzerland, 2022; pp. 173–186.

27. Kickingereder, P.; Isensee, F.; Tursunova, I.; Petersen, J.; Neuberger, U.; Bonekamp, D.; Brugnara, G.; Schell, M.; Kessler, T.; Foltyn, M.; et al. Automated Quantitative Tumour Response Assessment of MRI in Neuro-Oncology with Artificial Neural Networks: A Multicentre, Retrospective Study. *Lancet Oncol.* **2019**, *20*, 728–740. [CrossRef]

28. Isensee, F.; Jaeger, P.F.; Kohl, S.A.A.; Petersen, J.; Maier-Hein, K.H. NnU-Net: A Self-Configuring Method for Deep Learning-Based Biomedical Image Segmentation. *Nat. Methods* **2021**, *18*, 203–211. [CrossRef]

29. Zhang, Y.; Brady, M.; Smith, S. Segmentation of Brain MR Images through a Hidden Markov Random Field Model and the Expectation-Maximization Algorithm. *IEEE Trans. Med. Imaging* **2001**, *20*, 45–57. [CrossRef]

30. Klein, S.; Staring, M.; Murphy, K.; Viergever, M.A.; Pluim, J. Elastix: A Toolbox for Intensity-Based Medical Image Registration. *IEEE Trans. Med. Imaging* **2010**, *29*, 196–205. [CrossRef]

31. Reyes-Aldasoro, C.C.; Williams, L.J.; Akerman, S.; Kanthou, C.; Tozer, G.M. An Automatic Algorithm for the Segmentation and Morphological Analysis of Microvessels in Immunostained Histological Tumour Sections. *J. Microsc.* **2011**, *242*, 262–278. [CrossRef]

32. Smits, M.; van den Bent, M.J. Imaging Correlates of Adult Glioma Genotypes. *Radiology* **2017**, *284*, 316–331. [CrossRef]

33. Vanchinathan, V.; Mizramani, N.; Kantipudi, R.; Schwartz, E.J.; Sundram, U.N. The Vascular Marker CD31 Also Highlights Histiocytes and Histiocyte-Like Cells Within Cutaneous Tumors. *Am. J. Clin. Pathol.* **2015**, *143*, 177–185. [CrossRef] [PubMed]

34. Wesseling, P.; van der Laak, J.A.; Link, M.; Teepen, H.L.; Ruiter, D.J. Quantitative Analysis of Microvascular Changes in Diffuse Astrocytic Neoplasms with Increasing Grade of Malignancy. *Hum. Pathol.* **1998**, *29*, 352–358. [CrossRef]

35. Wesseling, P.; van der Laak, J.A.; de Leeuw, H.; Ruiter, D.J.; Burger, P.C. Quantitative Immunohistological Analysis of the Microvasculature in Untreated Human Glioblastoma Multiforme. Computer-Assisted Image Analysis of Whole-Tumor Sections. *J. Neurosurg.* **1994**, *81*, 902–909. [CrossRef] [PubMed]

36. Stewart, P.A.; Farrell, C.L.; del Maestro, R.F. The Effect of Cellular Microenvironment on Vessels in the Brain. Part 1: Vessel Structure in Tumour, Peritumour and Brain from Humans with Malignant Glioma. *Int. J. Radiat. Biol.* **1991**, *60*, 125–130. [CrossRef] [PubMed]

37. Li, X.; Morgan, P.S.; Ashburner, J.; Smith, J.; Rorden, C. The First Step for Neuroimaging Data Analysis: DICOM to NIfTI Conversion. *J. Neurosci. Methods* **2016**, *264*, 47–56. [CrossRef] [PubMed]

38. Tustison, N.J.; Avants, B.B.; Cook, P.A.; Zheng, Y.; Egan, A.; Yushkevich, P.A.; Gee, J.C. N4ITK: Improved N3 Bias Correction. *IEEE Trans. Med. Imaging* **2010**, *29*, 1310–1320. [CrossRef]

39. Isensee, F.; Schell, M.; Pflueger, I.; Brugnara, G.; Bonekamp, D.; Neuberger, U.; Wick, A.; Schlemmer, H.; Heiland, S.; Wick, W.; et al. Automated Brain Extraction of Multisequence MRI Using Artificial Neural Networks. *Hum. Brain Mapp.* **2019**, *40*, 4952–4964. [CrossRef]

40. Smith, S.M. Fast Robust Automated Brain Extraction. *Hum. Brain Mapp.* **2002**, *17*, 143–155. [CrossRef]

41. Fonov, V.; Evans, A.C.; Botteron, K.; Almli, C.R.; McKinstry, R.C.; Collins, D.L. Unbiased Average Age-Appropriate Atlases for Pediatric Studies. *Neuroimage* **2011**, *54*, 313–327. [CrossRef]

42. Shamonin, D. Fast Parallel Image Registration on CPU and GPU for Diagnostic Classification of Alzheimer's Disease. *Front. Neuroinformatics* **2013**, *7*, 50. [CrossRef]

43. Rohlfing, T.; Zahr, N.M.; Sullivan, E.v.; Pfefferbaum, A. The SRI24 Multichannel Atlas of Normal Adult Human Brain Structure. *Hum. Brain Mapp.* **2009**, *31*, 798–819. [CrossRef] [PubMed]

44. Rohlfing, T.; Russakoff, D.B.; Maurer, C.R. Performance-Based Classifier Combination in Atlas-Based Image Segmentation Using Expectation-Maximization Parameter Estimation. *IEEE Trans. Med. Imaging* **2004**, *23*, 983–994. [CrossRef] [PubMed]